International workshop on "LES for Acoustics"
7.-8. October 2002, DLR Göttingen, Germany

LES of the noise radiated by a flow over a rectangular cavity

Xavier Gloerfelt, Christophe Bogey and Christophe Bailly

Laboratoire de Mécanique des Fluides et d'Acoustique
Ecole Centrale de Lyon & UMR CNRS 5509
69134 Ecully, France.
http://www.lmfa.ec-lyon.fr/autres/CAA/caaweb.html

Abstract

The structure of an unsteady flow past a rectangular, open cavity is investigated using numerical simulations. Particular attention is drawn to the effects of the laminar or turbulent state of the incoming boundary layer. The consequences on noise generation are studied using Direct Noise Computation, solving the filtered 3-D compressible Navier-Stokes equations. The turbulence level and the shear strength before the separation corner are seen to influence the large-amplitude oscillations in the cavity.

1. Introduction

Cavity flows, characterized by a severe acoustic environment within and outside the cavity, arise from a feedback loop, locked in by the geometry and the flow characteristics. Extensive research efforts over the past 40 years have been devoted to the characterization of the mechanism giving rise to the self-sustained oscillations. This phenomenon governs the self-forced oscillations of a much larger class of flows where a shear layer impinges an obstacle.[1]

The feedback process is now well-established. The growth and convection of instability waves in the shear layer induce large-amplitude pressure disturbances as the vortical perturbations impinge the downstream corner of the cavity. The upstream influence of the generated pressure fluctuations provides further excitation of the instabilities in the shear layer, especially in its most receiptive region near the upstream edge. A stable phase criterion is then installed between the downstream and the upstream edges of the cavity, leading to a lock-in self-sustained state. This criterion is the basis of the Rossiter formula,[2] which predicts the admissible frequencies as a function of the length L of the cavity, the Mach number M of the flow, and an integer n, representing the number of vortices between the two corners of the cavity. For M$>$ 0.4, this semi-empirical formula succeeds in estimating the oscillation frequencies for either laminar or turbulent flows past the cavity. However, experimental observations for fully turbulent cases have not always indicated the presence of highly localized vortices. Besides, this kind of semi-empirical model is independent on the Reynolds number, and cannot describe the changes between an initially laminar or turbulent

incoming boundary layer, as evidenced in the early experiments of Karamcheti.[3] The latter observed a reduction in the amplitude of the pressure fluctuations and the emergence of a low-frequency component for a turbulent inflow in comparison with the initially laminar case. Demetz and Farabee[4] investigated the influence of the laminar or turbulent state of the inflow on an acoustically resonant cavity, and found some significant differences occurring in the coupling mechanism at the opening interface. A reduction in the pressure amplitudes is also noticeable. This property has been used recently for the control of the cavity oscillations through very high frequency forcing.[5] This forcing can drain energy out of the low frequencies, and dump this energy into the small scales, which induces a less coherent interaction with the downstream edge, and, consequently, reduces the acoustic emission. The visualizations of Lin and Rockwell,[6] using particle image velocimetry (PIV) technique for a fully turbulent boundary layer past a rectangular cavity in water, show the persistence of organized vortical structures, and a possible low-frequency modulation by the unsteady recirculating flow within the cavity.

In this study, we are also concerned with the influence of the laminar or turbulent state of the incoming boundary layer on the cavity oscillations and the acoustic radiated field. The Direct Computation of Noise (DCN) is used to probe this effects, and to give a more complete picture of the flow field. The 3-D compressible Navier-Stokes equations are solved directly using high-order algorithms to preserve the features of noise propagation. The boundaries are then chosen sufficiently far from the cavity to avoid self-forcing and to include a portion of the radiated field. The configuration of Karamcheti's study[3] with a length-to-depth ratio of 3 and a freestream Mach number 0.8 is simulated numerically with the same dimensions as in the experiment ($D = 2.54$ mm). To achieve reasonable computational cost, and using the fact that the cavity flow is dominated by the interactions of coherent structures with the upstream edge, Large Eddy Simulations (LES) are performed. The details of the computational modelling are described in the first part of the paper. The modifications of the flow field for intially laminar and turbulent inflow are then addressed, and the consequences on the radiated sound field are investigated in the last section.

2. Numerical methods

2.1 Governing equations

A schematic view of the flow domain is shown in figure 1. The origin of the coordinate system is located at the middle of the upstream corner. The governing equations are the unsteady compressible three-dimensional Navier-Stokes equations. They are expressed in a conservative form in the Cartesian coordinate system of figure 1. In Large Eddy Simulation, only the large-scale structures are computed explicitely, and the small scales are modelled. The governing equations are obtained after spatial filtering, denoted by a bar. The velocity components are decomposed into a resolved part, $\widetilde{u_i} = \overline{\rho u_i}/\overline{\rho}$, using Favre averaging, and an unresolved part, u_i''. The resulting system solved

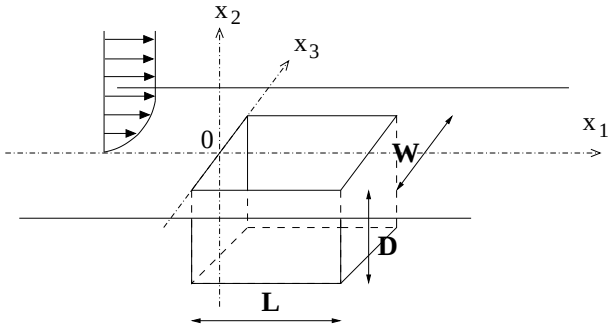

Figure 1: Sketch of the flow domain and coordinate system.

in the present study is :

$$\frac{\partial \mathbf{U}}{\partial t} + \frac{\partial \mathbf{E_e}}{\partial x_1} + \frac{\partial \mathbf{F_e}}{\partial x_2} + \frac{\partial \mathbf{G_e}}{\partial x_3} - \frac{\partial \mathbf{E_v}}{\partial x_1} - \frac{\partial \mathbf{F_v}}{\partial x_2} - \frac{\partial \mathbf{G_v}}{\partial x_3} = 0 \tag{1}$$

where:

$$\begin{aligned}
\mathbf{U} &= (\overline{\rho}, \overline{\rho}\widetilde{u_1}, \overline{\rho}\widetilde{u_2}, \overline{\rho}\widetilde{u_3}, \overline{\rho}\widetilde{e})^t \\
\mathbf{E_e} &= (\overline{\rho}\widetilde{u_1}, \widetilde{p} + \overline{\rho}\widetilde{u_1}^2, \overline{\rho}\widetilde{u_1}\widetilde{u_2}, \overline{\rho}\widetilde{u_1}\widetilde{u_3}, (\overline{\rho}\widetilde{e} + \widetilde{p})\widetilde{u_1})^t \\
\mathbf{F_e} &= (\overline{\rho}\widetilde{u_2}, \overline{\rho}\widetilde{u_2}\widetilde{u_1}, \widetilde{p} + \overline{\rho}\widetilde{u_2}^2, \overline{\rho}\widetilde{u_2}\widetilde{u_3}, (\overline{\rho}\widetilde{e} + \widetilde{p})\widetilde{u_2})^t \\
\mathbf{G_e} &= (\overline{\rho}\widetilde{u_3}, \overline{\rho}\widetilde{u_3}\widetilde{u_1}, \overline{\rho}\widetilde{u_3}\widetilde{u_2}, \widetilde{p} + \overline{\rho}\widetilde{u_3}^2, (\overline{\rho}\widetilde{e} + \widetilde{p})\widetilde{u_3})^t \\
\mathbf{E_v} &= (0, \widetilde{\tau_{11}} + \mathcal{T}_{11}, \widetilde{\tau_{12}} + \mathcal{T}_{12}, \widetilde{\tau_{13}} + \mathcal{T}_{13}, \widetilde{u_i}(\widetilde{\tau_{1i}} + \mathcal{T}_{1i}) - \widetilde{q_1} - c_v\mathcal{Q}_1)^t \\
\mathbf{F_v} &= (0, \widetilde{\tau_{21}} + \mathcal{T}_{21}, \widetilde{\tau_{22}} + \mathcal{T}_{22}, \widetilde{\tau_{23}} + \mathcal{T}_{23}, \widetilde{u_i}(\widetilde{\tau_{2i}} + \mathcal{T}_{2i}) - \widetilde{q_2} - c_v\mathcal{Q}_2)^t \\
\mathbf{G_v} &= (0, \widetilde{\tau_{31}} + \mathcal{T}_{31}, \widetilde{\tau_{32}} + \mathcal{T}_{32}, \widetilde{\tau_{33}} + \mathcal{T}_{33}, \widetilde{u_i}(\widetilde{\tau_{3i}} + \mathcal{T}_{3i}) - \widetilde{q_3} - c_v\mathcal{Q}_3)^t
\end{aligned}$$

where c_v is the specific heat at constant volume. The quantities $\overline{\rho}$, $\widetilde{p}$, $\widetilde{u_i}$ are the density, pressure, and velocity components. For a perfect gas, the total energy per mass unit $\widetilde{e}$ is :

$$\widetilde{e} = \widetilde{p}/[(\gamma-1)\overline{\rho}] + (\widetilde{u_1}^2 + \widetilde{u_2}^2 + \widetilde{u_3}^2)/2, \quad \text{and} \quad \widetilde{p} = r\overline{\rho}\widetilde{T},$$

where $\widetilde{T}$ is the temperature, r the gas constant, and γ the ratio of specific heats. The viscous stress tensor $\widetilde{\tau_{ij}}$ is modelled as a Newtonian fluid $\widetilde{\tau_{ij}} = 2\mu\widetilde{S_{ij}}$, where μ is the dynamic molecular viscosity, and $\widetilde{S_{ij}}$ the deviatoric part of the resolved deformation stress tensor :

$$\widetilde{S_{ij}} = \frac{1}{2}\left(\frac{\partial \widetilde{u_i}}{\partial x_j} + \frac{\partial \widetilde{u_j}}{\partial x_i} - \frac{2}{3}\delta_{ij}\frac{\partial \widetilde{u_k}}{\partial x_k}\right)$$

The heat flux component $\widetilde{q_i}$ models thermal conduction in the flow with Fourier's law $\widetilde{q_i} = -(\mu c_p/\sigma)(\partial\widetilde{T}/\partial x_i)$, where σ is the Prandtl number, and c_p the specific heat at constant pressure.

Subgrid modelling

The effects of the fine scales are present in system (1) through the subgrid scale stress tensor $\mathcal{T}_{ij}$ and the subgrid scale heat flux $\mathcal{Q}_i$, respectively :

$$\mathcal{T}_{ij} = -\overline{\rho}(\widetilde{u_i u_j} - \widetilde{u_i}\widetilde{u_j}), \qquad \mathcal{Q}_i = \overline{\rho}(\widetilde{u_i T} - \widetilde{u_i}\widetilde{T})$$

The simple closure model consists in reproducing the dissipative effets of the unresolved scales by incorporating a turbulent viscosity μ_t, a subgrid scale energy k_{sgs}, and a turbulent Prandtl number σ_t. The subgrid scale tensor and heat flux can then be modelized by :

$$\mathcal{T}_{ij} = 2\mu_t \widetilde{S_{ij}} - \frac{2}{3}\overline{\rho} k_{sgs}\delta_{ij}, \qquad \mathcal{Q}_i = -\frac{\mu_t}{\sigma_t}\frac{\partial \widetilde{T}}{\partial x_i}$$

We choose the Smagorinsky eddy-viscosity model, where $\mu_t = \overline{\rho}(C_S\Delta_c)^2\sqrt{2\widetilde{S}_{ij}\widetilde{S}_{ij}}$, C_S is the Smagorinsky constant, and Δ_c the characteristic length scale, $\Delta_c = (\Delta x_1 \Delta x_2 \Delta x_3)^{1/3}$. The unaltered value $C_S = 0.18$ is taken, representing the dissipation associated to the small unresolved turbulent scales in an isotropic turbulence. The subgrid scale energy k_{sgs} is not directly available, but, following Erlebacher *et al.*,[7] the isotropic part is considered to be dominated by the pressure, so that $k_{sgs} = 2C_I\overline{\rho}\Delta_c^2\widetilde{S}_{ij}\widetilde{S}_{ij}$, where $C_I \simeq 0.1$ is the energy constant. Endly, the turbulent Prandtl number is taken constant, $\sigma_t \simeq 0.1$.

Wall model

One of the major drawback of the previous modelling is that the Smagorinsky model is not able to describe the scale reduction that occurs near the solid walls. The simpliest solution consists in superimposing an empirical wall law near the solid boundaries. Moin et Kim[8] and several authors propose to multiply the characteristic length scale Δ_c by the exponential van Driest damping function :

$$\Delta_c' = \left\{1 - \exp\left(\frac{x_2^+}{A^+}\right)\right\}(\Delta x_1 \Delta x_2 \Delta x_3)^{1/3}$$

where $A^+ = 25$ and $x_2^+ = x_2 u_\tau/\nu$ is the normal wall coordinate. The friction speed u_τ is determined by solving the logarithmic law :

$$\frac{\widetilde{u_{1_0}}(x_2)}{u_\tau} - 5.75\log\left(\frac{x_2 u_\tau}{\nu}\right) + 5.24 = 0$$

with $\widetilde{u_{1_0}}$ designing the mean longitudinal velocity and ν the kinematic viscosity.

The effects of the turbulent modelling are only briefly entered upon in this study. Its choice was essentially motivated by its reduced numerical cost. It is only used for the fully turbulent simulation. A comparison with and without model is also performed to assess the relative independence on the turbulent viscosity model. The evaluation of the model effects can only be made possible if quantitative experimental data were available. No model is employed for the initially laminar case since the standard Smagorinsky is not able to describe the transition to turbulence.

2.2 Algorithm and boundary conditions

Algorithm

The governing equations (1) are integrated in time using an explicit low-storage six-step Runge-Kutta scheme, optimized in the wave number space, for the convective terms. Because of their slower time evolution, the viscous terms are integrated in the last substep without affecting the

global accuracy. The gradients are solved on the rectangular nonuniform grid by using optimized finite difference coefficients for an eleven-point stencil for the convective fluxes, and 4^{th} order finite differences for the viscous and heat fluxes. As part of the algorithm, a selective damping term built on an eleven-point stencil is incorporated in each direction to eliminate numerical oscillations originating from regions with large gradients and/or from the boundary treatment. The coefficients of the Runge-Kutta, of the finite differences and of the damping schemes are given in Bogey and Bailly.[9]

Solid walls

On all solid boundaries, the no-slip conditions $\widetilde{u_1} = \widetilde{u_2} = \widetilde{u_3} = 0$ are imposed, with $\partial\widetilde{p}/\partial n = 0$, where n is the direction normal to the rigid surface. The wall temperature is calculated by using the adiabatic condition. For the sharp corners formed by the intersection of planar cavity surfaces, the variables are determined by using the interior scheme, thereby avoiding any ambiguity regarding the normal direction.

Radiation conditions

At the upstream and upper boundaries, the radiation boundary conditions of Tam and Dong,[10] using a far-field solution of the linearized Euler equations, are applied. At the outflow, we combine the outflow boundary conditions of Tam and Dong, where the far-field solution is modified to allow the exit of vortical and entropic disturbances, with a sponge zone to dissipate vortical structures. This sponge zone uses grid stretching and a progressively applied Laplacian filter.

Lateral boundaries

The treatment of the lateral boundaries raises serious problems for an aeroacoustic simulation. The most common choice in CFD calculations is the use of either periodic, symmetric conditions, or slip walls. They are precluded for an acoustic calculation because they reflect acoustic waves. Therefore we modelize the two sidewalls like other rigid wall conditions. The lateral boundaries above the cavity are then free boundaries, where the non-reflecting condition combined with a sponge zone is used.

Method of generating inflow turbulence

To create the unsteady, stochastic inflow condition for spatial turbulent simulations, we use Random Fourier Modes (RFM), following the construction of the SNGR model.[11] The turbulent inlet field is generated by the sum of N independent RFM, with amplitudes $\hat{u}_n$ determined from the turbulent kinetic energy spectrum. The fluctuating velocity field is then expressed as a Fourier series :

$$\mathbf{u}'(\mathbf{x},t) = \sum_{n=1}^{N} \hat{u}_n \cos(\mathbf{k}_n.(\mathbf{x} - \widetilde{\mathbf{u}_0}t) + \omega_n t + \psi_n)\mathbf{a}_n$$

where ψ_n, $\mathbf{k}_n$, $\mathbf{a}_n$ are random variables with given probability density functions. An unfrozen turbulent field is obtained by incorporating the convection velocity $\widetilde{\mathbf{u}_0}$ and the pulsation ω_n, ac-

counting for the temporal evolution of the perturbations. In the present turbulent simulation, we have taken $N = 200$ RFM and ω_n is deduced from the Heisenberg time, $\omega_n = 2\pi u' k_n$, where u' is the rms fluctuating velocity and k_n the wave number. This stochastic velocity field is multiplied by the vertical profiles of rms velocities from Spalart's[12] temporal DNS at $\mathrm{Re}_{\delta_\theta} = 1410$. This procedure gives the correct vertical distributions but has two drawbacks. First, the incompressibility condition is no longer ensured and the excitation becomes noisy. This spurious radiation is however sufficiently weak compared to cavity noise. Second, it cannot provide the phase relationship between individual Fourier modes, and turbulence decays downstream of the inlet plane until the near wall cycle of turbulence production has been established. Nevertheless, the temporal evolution through Heisenberg's time allows a very quick by-pass transition to turbulence.

2.3 Simulation parameters

Flow configurations

Run	Aspect ratio		Mach	Re_D	$\mathrm{Re}_{\delta_{\theta_R}}$	H	Régime	Model
	L/D	L/W						
3Dr3L	3	0.78	0.8	48600	990	2.3	lam.	no model
3Dr3Ts	3	0.78	0.8	48600	2250	1.9	turb.	SM
3Dr3Tn	3	0.78	0.8	48600	2250	1.9	turb.	no model

Table 1: Recapitulative table of the simulation parameters. SM = Smagorinsky model. H is the shape factor, $H = \delta_{\theta_R}/\delta^*_R$. The thicknesses (suffix R) are evaluated at the upstream edge of the cavity when the mean flow is converged.

The three simulations performed are summarized in table 1. They match two configurations of Karamcheti's experiments.[3] The computations are initialized with a given velocity profile $u_{1_0}(x_2)$, found for the inflow, and extrapolated into the entire computational domain. u_{2_0} and u_{3_0} are set to zero, the freestream air temperature is $T_\infty = 320.26$ K, and the static pressure p_∞ is taken as 1 atm. For the initially laminar inflow configurations, $u_{1_0}(x_2)$ corresponds to a third order polynomial expression of the Blasius profile, and no forcing is applied. For the initially turbulent simulation, the mean profile at the inlet is obtained from Spalart's[12] temporal boundary layer simulation at $\mathrm{Re}_{\delta_\theta} = 1410$, to which inflow turbulence, generated by the method described in §2.2, is superimposed.

Numerical specifications

The computational mesh is nonuniform and Cartesian, with $87 \times 71 \times 123$ grid points inside the cavity and $235 \times 130 \times 151$ outside, refined near the walls. The size of the computational domain is $12.8D \times 7.8D \times 5.2D$. For explicit time marching schemes, the time step must satisfy the CFL stability criterion, $\Delta t = 1. \times \Delta x_{2_{min}}/c_\infty = 5.8 \times 10^{-8}$ s, and a large number of time iterations is needed. Each computation lasts 40 hours on a Nec SX-5, for 5.4 million grid-points (CPU time of 0.6 μs per grid point and per iteration).

3. Laminar and turbulent boundary layers ahead of the cavity

3.1 Vorticity field

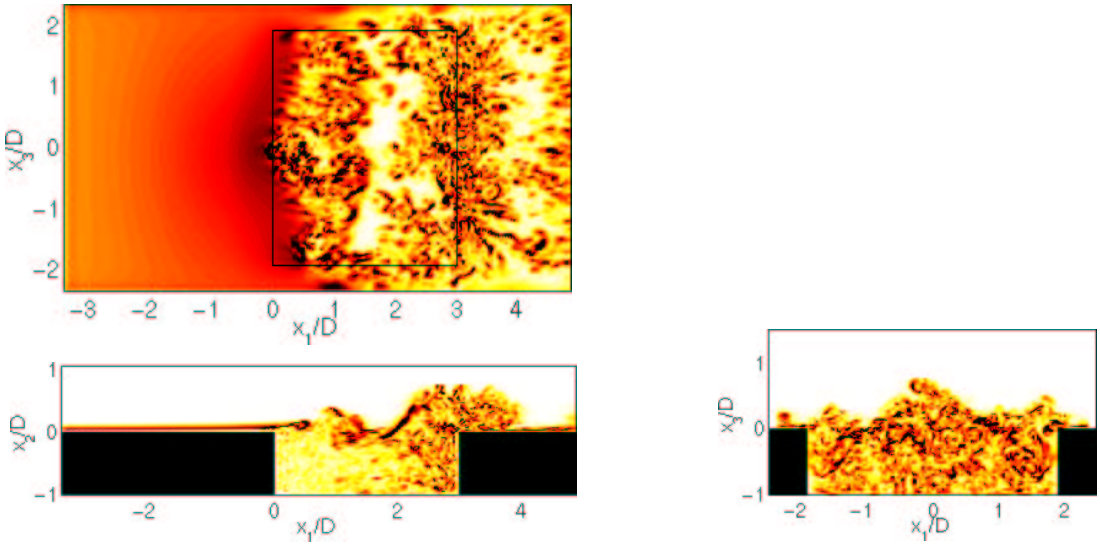

Figure 2: Snapshot of vorticity modulus $\|\boldsymbol{\omega}\|$ in run 3Dr3L. From top to bottom, side view at $x_3 = 0$, top view at $x_2/D = 0.06$, and cross section at $x_1/D = 3.9$.

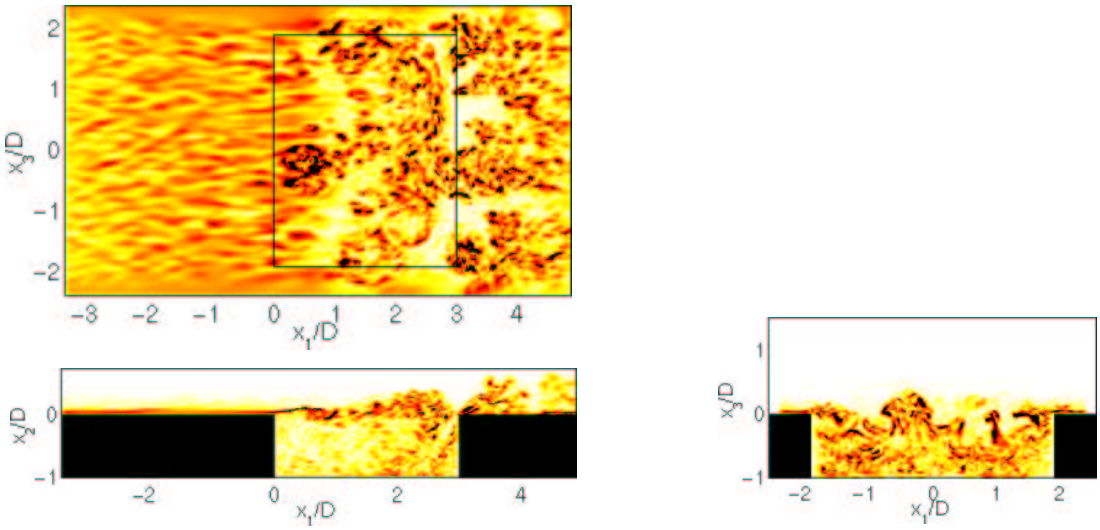

Figure 3: Snapshot of vorticity modulus $\|\boldsymbol{\omega}\|$ in run 3Dr3Ts. From top to bottom, side view at $x_3 = 0$, top view at $x_2/D = 0.06$, and cross section at $x_1/D = 3.9$.

As shown by the snapshots of vorticity of figures 2 and 3, large-scale vortices emerge from the turbulent background. These vortices are actually made up of a number of small-scales vortices. The centers of the coherent structures for the turbulent inflow are below those found for the laminar inflow, in agreement with the observations of Demetz and Farabee.[4] A further study of the flow structures indicates that the clusters of small scales are clipped as they impinge on the corner and

travel down along the vertical surface, then upstream along the cavity floor, resulting in a wall jet-like flow.[6] Unsteadiness of this upward-oriented jet contributes to the modulated character of the separated shear layer.

The spanwise structure of the free-shear layer along the mouth of the cavity is visualized in top views and reveals the interaction of secondary (longitudinal) and primary (Kelvin-Helmholtz) vorticity. These observations are consistent with Rockwell and Knisely[13] visualizations using the hydrogen bubble technique. The interaction between streamwise vorticity and primary spanwise rolls enhances the mixing, and was postulated as the basis of the energy cascade towards smaller scales. Mushroom-shaped ejections are exhibited in the cross section of figure 3, as in the visualizations of Bernal and Roshko.[14] This is characteristic of streamwise vortices. Their tendency to move away in the radial direction is associated with curvature of the streamwise vortices imposed by the primary spanwise rolls.

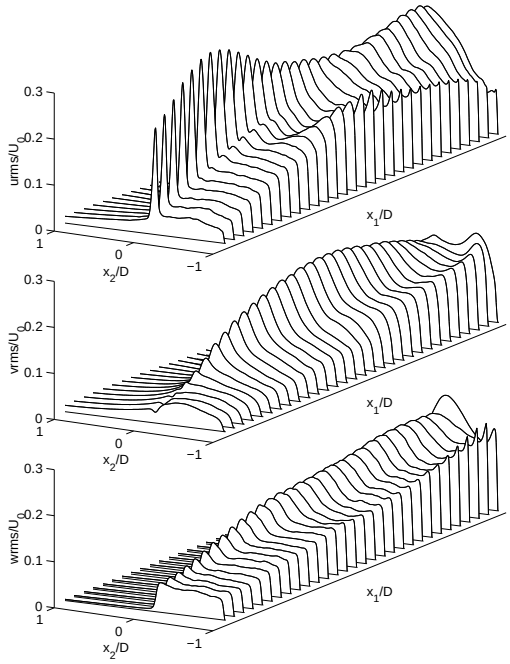

(a)

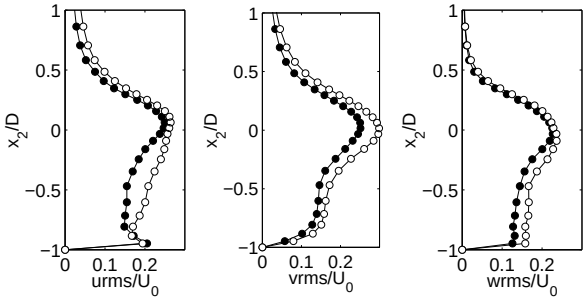

(b)

	u_{rms}	v_{rms}	w_{rms}	$d\delta_\theta/dx_1$
3Dr3L	0.35	0.30	0.28	0.03
3Dr3Ts	0.27	0.25	0.26	0.03
Forestier[15]	0.23	0.23	-	0.035-0.07
Oster & Wygnanski[16]	0.21	0.3	-	0.02

Figure 4: (a) : *rms* fluctuating velocities statistics for 3Dr3L simulation. Profiles made every $L/30$ between $x_1 = 0$ and $x_1 = L$. (b) : comparison of *rms* velocity profiles at the location $x_1 = 2L/3$ for the 3Dr3Ts (-•-) and 3Dr3L (-○-) simulations. Maximal values of *rms* velocity fluctuations and estimation of spreading rates are given in the table.

3.2 Turbulence intensities

The *rms* fluctuating velocity profiles are given in figure 4(a) for the initially laminar case. The single peak distributions are enlarged by the randomness of small-scales. They can even encompass all the cavity depth further downstream, illustrating the relationship between the shear

layer and the recirculating flow within the cavity. Their amplitude is relatively high (about 30 %) but are not given in Karamcheti's experiment for comparison. The most striking point concerns the development of the spanwise fluctuations, which reach the same amplitude as the two other components. The cavity flow is now highly turbulent and three dimensional. The comparison of the laminar and turbulent simulations in figure 4(b) reveals that the levels are slightly higher for the laminar case (see maximum values in table of figure 4). In this case the intensity of u_{rms} reaches a maximum soon after the leading edge. It eventually stabilizes further downstream around an asymptotic value due to small-scale transition. The intensity of the fluctuation peak for the turbulent incoming boundary layer relaxes monotonically to approximately the same value as in the laminar boundary-layer case, but there is no overshoot.

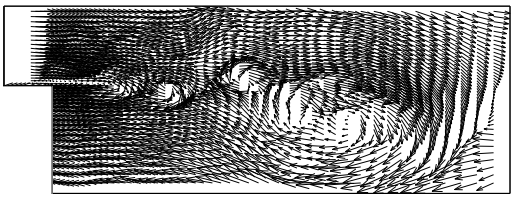

Figure 5: Zoom of velocity field around the upstream corner of the cavity for the turbulent simulation.

3.3 Collective interaction

Figure 5 displays the early development of the shear layer. The initial shedding frequency is around $\mathrm{St}_\theta = 0.017$, which is close to the most unstable frequency predicted by the linear theory of stability. Further downstream the flow contains larger structures (i.e. lower frequency components). This frequency drop is associated with the successive or simultaneous coalescence of a number of vortices, referred to as collective interaction by Ho et Nosseir.[17] The low-frequency component (due to the upstream acoustic waves) forces the shear layer to undulate, and the vortices, shedded at the initial instability frequency, are displaced laterally. Owing to their induced field, the vortices are drawn together and coalesce into a large vortex (see figure 5). This process depends obviously on the viscosity, and can therefore be influenced by the turbulent model. The passage frequency of the resulting coherent structure is equal to the forcing frequency. This phenomenon participates in the selection of a single frequency, characteristic of flow with self-sustained oscillations. The necessary condition for this interaction is a high-amplitude low-frequency excitation, provided here by the intense acoustic field. The two principal consequences are the drop in passage frequency and a high spreading rate for the shear layer.

4. Influence of the state of the incoming boundary layer on the radiated field

4.1 Spectra

The acoustic spectra for the turbulent 3Dr3Ts and laminar 3Dr3L cases are depicted in figure

6(a), and the predominance of the Strouhal number St=0.75 is observed in both cases. The integrated sound pressure level is 152 dB for the initially laminar case and 149 dB in the initially turbulent simulation 3Dr3Ts. This trend is conform to Karamcheti's results.[3] The latter noted a slightly lower frequency St=0.68 for the turbulent upstream boundary layer, and the intermittency with a low-frequency component St=0.33, which are not reproduced in our simulations. This is certainly attributable to the narrower width of the cavity investigated in the present simulation.

To ensure that this reduction in the radiated acoustic amplitude is not determined by the use of the turbulent viscosity model, a third simulation 3Dr3Tn has been performed with the same turbulent boundary layer inflow but with no model. The comparison of acoustic spectra for 3Dr3Ts and 3Dr3Tn, in figure 6(b), indicates that the levels are lower without the model (144 dB). The tendency is thus reinforced for the turbulent case without subgrid scale model. The results show also the emergence of the low-frequency component, as in Karamcheti's measurements. The turbulent viscosity in the Smagorinsky model appears to exert a strong influence on the shear layer behaviour and should require further investigations.

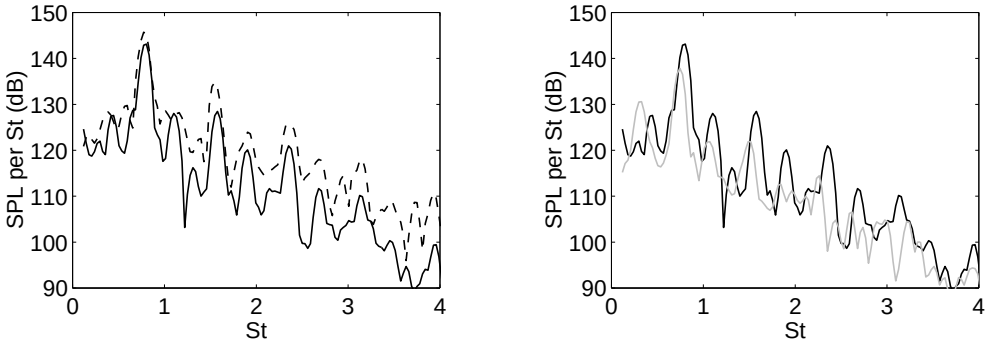

(a) (b)

Figure 6: Spectra of pressure fluctuations at $x_1/D = -1.04$ and $x_2/D = 4.64$ versus the Strouhal number : (a) : (——), 3Dr3Ts run and (– – –), 3Dr3L run. (b) : (——), 3Dr3Ts run and (——), 3Dr3Tn run.

4.2 Pressure field

The structure of the radiated field in figure 7 shows a strong downstream directivity due to the convection of acoustic wave fronts by the mean flow combined with the reflections on the cavity walls, resulting in different wave patterns. These pressure fields clearly illustrate the higher amplitude of the acoustic waves for the 3Dr3L simulation. The cross cuts show that sound waves are more two-dimensional in this case, whereas the fully turbulent cavity 3Dr3Ts generates three-dimensional nonuniformities indicating a less coherent behaviour of the oscillations. The more coherent case leads to the appearance of important higher harmonics in the radiated field (see figure 6), arising from the nonlinear distorsion.

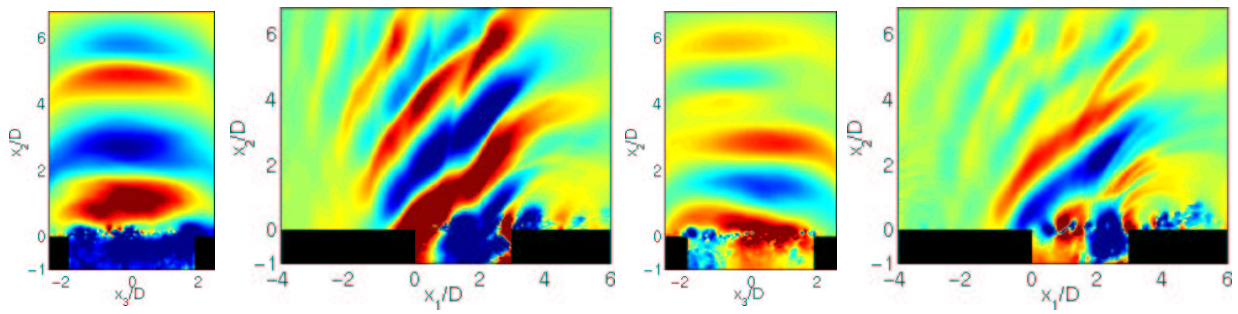

(a) (b) (c) (d)

Figure 7: Pressure fields for the run 3Dr3L (top), and run 3Dr3Ts (bottom). Right : longitudinal views in the $x_3 = 0$ plane. Left : cross views at $x_1/D = 2.9$, just before the downstream wall. Levels between -3000 and 3000 Pa.

5. Conclusion

The principal observation in this study concerns the influence of the laminar or turbulent state of the incoming boundary layer on the cavity oscillations. Organized vortical structures are visible in both cases but the amplitude of the pressure fluctuations are reduced for the turbulent inflow. These losses in coherence affect the strength of the upstream influence, and consequently the amplitude of the acoustic emission.

Concerning the numerical methods, the Direct Computation of Noise is demonstrated for 3-D cavity flows by considering the real spanwise extent of the rectangular cavity. The method for generating inflow turbulence allows the quick spatial development of the boundary layer. The role of preexisting vortical structures in the approach turbulent boundary layer remains for further investigations.

Besides, the collective interaction after the upstream corner is of fundamental interest in the process of selection of the main oscillation frequency. It depends on the level of forcing, on the ratio L/δ_θ, and also on the level of the turbulent viscosity, which is seen to have a significant influence on the shear-layer development.

Acknowledgments

Supercomputer time is supplied by Institut du Développement et des Ressources en Informatique Scientifique (IDRIS - CNRS).

References

[1]Rockwell, D. & Naudascher, E., 1979, Self-sustained oscillations of impinging free shear layer, *Ann. Rev. Fluid Mech.*, **11**, p. 67–94.

[2]Rossiter, J.E. Wind-tunnel experiments on the flow over rectangular cavities at subsonic and transonic speeds. Technical Report 3438, *Aeronautical Research Council Reports and Memoranda*, 1964.

[3]Karamcheti, K. Acoustic radiation from two-dimensional rectangular cutouts in aerodynamic surfaces. *Tech. Note* 3487, NACA, 1955.

[4]DeMetz, F.C. & Farabee, T.M., 1977, Laminar and turbulent shear flow induced cavity resonance, *AIAA Paper 77-1293*.

[5]Stanek, M.J., Raman, G., Kibens, V., Ross, J.A., Odedra, J. & Peto, J.W., 2000, Control of cavity resonance through very high frequency forcing, *AIAA Paper 2000-1905*.

[6]Lin, J.C. & Rockwell, D., 2001, Organized oscillations of initially turbulent flow past a cavity, *AIAA Journal*, **39**(6), p. 1139–1151.

[7]Erlebacher, G., Hussaini, M.Y., Speziale, C.G. & Zang, T.A., 1992, Toward the large-eddy simulation of compressible turbulent flows, *J. Fluid Mech.*, p. 155–185.

[8]Moin, P. & Kim, J., 1982, Numerical investigation of turbulent channel flow, *J. Fluid Mech.*, **118**, p. 341–377.

[9]Bogey, C. & Bailly, C., 2002, A family of low dispersive and low dissipative explicit schemes for computing aerodynamic, *AIAA Paper 2002-2509*.

[10]Bogey, C. & Bailly, C., 2002, Three-dimensional non-reflective boundary conditions for acoustic simulations : far field formulation and validation test cases, *Acta Acustica*, **88**, p. 463–471.

[11]Bailly, C., Lafon, P. & Candel, S., 1995, A stochastic approach to compute noise generation and radiation of free turbulent flows, *AIAA Paper 95-092*.

[12]Spalart, P.R., 1988, Direct simulation of a turbulent boundary layer up to $R_\theta = 1410$, *J. Fluid Mech.*, **187**, p. 61–98.

[13]Rockwell, D. & Knisely, C., 1980, Observations of the three-dimensional nature of instable flow past a cavity, *Phys. Fluids*, **23**(3), p. 425–431.

[14]Bernal, L.P. & Roshko, A., 1986, Streamwise vortex structure in plane mixing layers, *J. Fluid Mech.*, **170**, p. 499–525.

[15]Forestier, N. *Etude expérimentale d'une couche cisaillée au-dessus d'une cavité en régime transonique*. PhD thesis, Ecole Centrale de Lyon, 2001. No NT 2001-1.

[16]Oster, D. & Wygnanski, I., 1982, The forced mixing layer between parallel streams, *J. Fluid Mech.*, **123**, p. 91–130.

[17]Ho, C.-M. & Nosseir, N.S., 1981, Dynamics of an impinging jet. Part 1. The feedback phenomenon, *J. Fluid Mech.*, **105**, p. 119–142.